



Article

Diurnal Variation Characteristics of Summer Precipitation over the Northern Slope of the Tianshan Mountains, Xinjiang, Northwest China: Basic Features and Responses to the Inhomogeneous Underlying Surface

Zulipina Kadier ^{1,†}, Zhiyi Li ^{1,†}, Abuduwaili Abulikemu ^{1,*} , Kefeng Zhu ², Aierzuna Abulimiti ¹, Dawei An ³ and Abidan Abuduaini ¹

¹ Xinjiang Key Laboratory of Oasis Ecology, College of Geography and Remote Sensing Sciences, Xinjiang University, Urumqi 830017, China; zulipinakadier@stu.xju.edu.cn (Z.K.); lizhiyi@stu.xju.edu.cn (Z.L.); aierzuna@stu.xju.edu.cn (A.A.); abidaabdugini@stu.xju.edu.cn (A.A.)

² Key Laboratory of Transportation Meteorology of China Meteorological Administration, Nanjing Joint Institute for Atmospheric Sciences, Nanjing 210041, China; zhukf@cma.gov.cn

³ Xinjiang Meteorological Observatory, Urumqi 830002, China; andawei817582@cma.com

* Correspondence: abduwaly@xju.edu.cn

† These authors contributed equally to this work.

Abstract: The diurnal variation characteristics of precipitation in summer (June–August) during the period of 2015–2019 over the Northern Slope of the Tianshan Mountains (NSTM) was analyzed using hourly simulated data from Nanjing University’s real-time forecasting system (WRF_NJU) with 4 km resolution, Automatic Weather Station (AWS) data, and the ERA5-Land data through using methods such as the Rotated Empirical Orthogonal Function (REOF) and Coefficient of Variation (CV). The results show that the diurnal variation pattern of the precipitation over the NSTM simulated by WRF_NJU aligns closely with that of the observational AWS data, and it captured spatial distribution, peak values, and the times of precipitation reasonably well. The hourly precipitation amount (PA), precipitation frequency (PF), and precipitation intensity (PI) all show characteristics of being greater in the afternoon to nighttime than from early morning to noon, and the diurnal variations of precipitation in this region are significantly influenced by altitude. The PA, PF, and PI peak over the southern edge of the Junggar Basin (JB) below 1000 m occurred at around 2200 Local Solar Time (LST). In contrast, peak PA over the mountainous regions above 3000 m occurred at around 1500 LST. Further analysis with REOF and CV indicated that the difference in diurnal variations of precipitation between the mountainous regions and the JB is most pronounced likely due to the topographical influences. The peak PA over the mountainous regions mainly occurred at around 1500 LST, while that of the JB occurred at around 0100 LST. High CV regions for PI are predominantly found over the area near the central JB and the middle Tianshan mountains, whereas high CV regions for the PF are located in the central and northern parts of Urumqi and Changji. In addition, different land surface categories exhibit distinct patterns of diurnal precipitation variation, i.e., the forests, grasslands, and water bodies exhibit their peak PA in the period from early morning to noon, while the impervious surfaces, croplands, and barren lands exhibit their peak PA in the period from afternoon to nighttime.

Keywords: diurnal variation; peak value; northern slope of Tianshan mountains; REOF; CV



Citation: Kadier, Z.; Li, Z.; Abulikemu, A.; Zhu, K.; Abulimiti, A.; An, D.; Abuduaini, A. Diurnal Variation Characteristics of Summer Precipitation over the Northern Slope of the Tianshan Mountains, Xinjiang, Northwest China: Basic Features and Responses to the Inhomogeneous Underlying Surface. *Remote Sens.* **2023**, *15*, 4833. <https://doi.org/10.3390/rs15194833>

Academic Editors: Xiefei Zhi, Donglian Sun, Wen Huo, Fei Ge and Jingyu Wang

Received: 29 August 2023

Revised: 27 September 2023

Accepted: 29 September 2023

Published: 5 October 2023



Copyright: © 2023 by the authors. Licensee MDPI, Basel, Switzerland. This article is an open access article distributed under the terms and conditions of the Creative Commons Attribution (CC BY) license (<https://creativecommons.org/licenses/by/4.0/>).

1. Introduction

The diurnal variation characteristics of precipitation stand out as one of the prominent natural cycles within Earth’s climate system [1,2]. Primarily stemming from discrete fluctuations in solar radiation, the resultant variations in pressure, wind, temperature, and numerous other factors collectively shape the distinctive features of the diurnal variations of precipitation [3,4]. According to the Sixth Assessment Report from the Intergovernmental

Panel on Climate Change (IPCC), the unprecedented rate of global warming has already led to a temperature increase of 1.1 °C compared to the 1850–1990 period [5]. This kind of rapid temperature escalation directly influences the hydrological cycle, causing significant shifts in precipitation and evaporation processes [6,7]. Consequently, the frequency of extreme weather and climate events (such as floods, extreme storms, heat waves, droughts, heavy precipitations, etc.) are on the rise as well [6,8]. These have far-reaching consequences, profoundly affecting human activities, natural environments, and ecosystems [9–12]. In light of these circumstances, comprehensive investigations into the variation characteristics of precipitation and the environmental factors influencing precipitation have become increasingly important.

Extensive investigations into the characteristics of diurnal variations in precipitation have been conducted worldwide using meteorological station data and satellite observation data. For example, Xiao et al. [13] conducted a study on diurnal variations in precipitation in the United Kingdom, and their results revealed that rainfall events lasting from 1 to 6 hours typically reach their peak intensity in the late afternoon. In two other studies, the distribution and propagation characteristics of precipitation was investigated during the warm seasons in North America and Southeast Asia [14,15]. Their findings indicated that the precipitation tends to originate over local mountains in the afternoon before propagating eastward or southeastward, reaching adjacent basins during the nighttime or in the early hours of the morning. Overall, previous research based on meteorological weather station observations and satellite data indicates significant diurnal variations in warm-season precipitation. Except for central USA and certain regions where precipitation peaks occur in the early morning, the majority of terrestrial regions globally experience precipitation peaks in the late afternoon or evening.

The diurnal variation characteristics of precipitation, as an important regional weather and climate characteristic, exhibit particularly noticeable differences under inhomogeneous or complex underlying surfaces. For instance, Dai et al. [4] conducted a regional study on the diurnal variation characteristics of precipitation in the United States and found that in the Southeast and Rocky Mountains, the maximum precipitation occurs in the evening, while it reaches its peak around midnight in the vicinity of plains. Tanaka et al. [16] analyzed the diurnal variation characteristics of precipitation in four stations with different land surface categories in the Manus region in the Amazon basin. Their results indicated that the higher precipitation over water vapor availability over the forest canopy is due to transpiration. As a result, the daytime rainfall is more frequent than nighttime rainfall, and the precipitation frequency at forest stations is significantly higher than that at urban stations.

In China, summer precipitation is influenced by complex terrain, leading to significant regional differences in the diurnal variation characteristics of precipitation across different regions. For example, Li et al. [17] conducted some studies on the diurnal variation characteristics of summer precipitation in the Qilian Mountains and the Qinghai–Tibet Plateau. Their results showed that the Qilian Mountains exhibit a bimodal precipitation pattern, with peaks occurring in the evening and early morning, while most stations in the Qinghai–Tibet Plateau experience precipitation peaks around evening or midnight. Yao et al. [18] analyzed the diurnal variation characteristics of precipitation using hourly meteorological station observation data in the Yangtze River Delta urban agglomeration for a period of 40 years. Their results indicated that the increase in long-duration and very-long-duration rainfall in urban regions is smaller compared to rural regions when moving from plains to mountains. In addition, Fu et al. [19] studied the tempo-spatial variation characteristics of summer precipitation and its relationship with urbanization in three super city clusters in eastern China using CMORPH data for a five-year period. They found that rainfall is primarily significant in mountainous regions with high frequency, while the plain regions surrounding the urban clusters experience higher hourly precipitation intensities. There are more (less) heavy rainfall (light rainfall) events in the upwind or downwind sides of the urban clusters.

The northern slope of the Tianshan Mountains (NSTM) is located in the northern part of Xinjiang, where the terrain gradually descends in elevation from south to north, and the Tianshan Mountains in the study area include the Middle Tianshan Mountains (MTM) and Eastern Tianshan Mountains (ETM), as shown in Figure 1a. The natural landscape undergoes a transitional change characterized by a “mountains–plain oasis–desert oasis–desert” pattern from the south to north over the region of the NSTM (Figure 1c). The primary land cover categories over the NSTM are grassland, bare land, and croplands, collectively accounting for 93.26% of the total land surface cover. Among them, grassland has the highest proportion (42.30%) [20]. The NSTM is centered around major cities such as Urumqi, Changji, Shihezi, and Karamay; the region forms Xinjiang’s largest urban cluster, as illustrated in Figure 1b. This urban cluster holds a prominent strategic position in the “Belt and Road” initiatives of China and stands as the most economically developed region in Xinjiang [21]. Over the years, it has contributed more than 40% of Xinjiang’s GDP [22] while also serving as the most densely populated region, with its urbanization rate increasing from 65.8% in 2000 to 79.9% in 2016 [23].

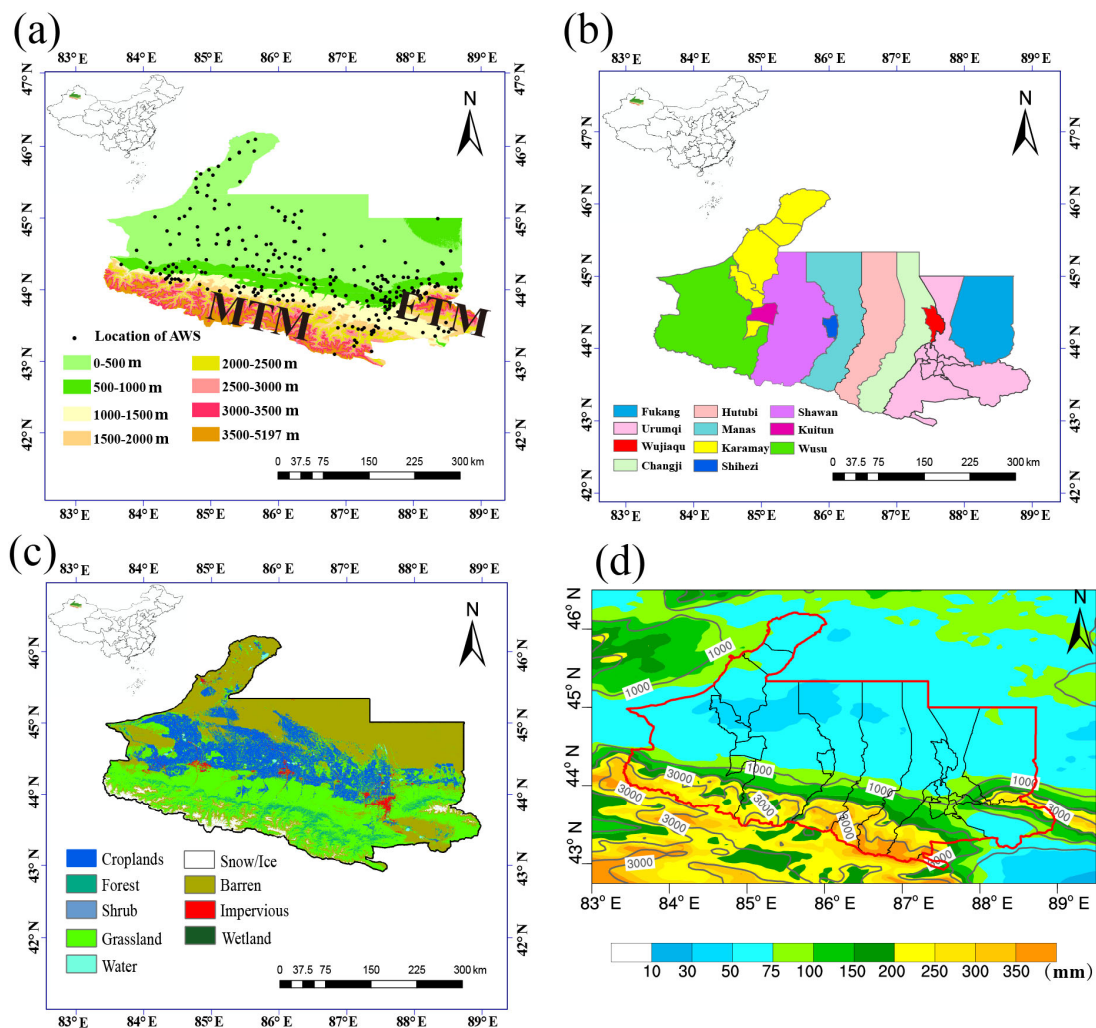


Figure 1. Overview of the study area. (a) Surface altitude (shading, units: m), distributions of the AWSs (indicated by black bots), along with labeling of the Eastern Tianshan Mountains (ETM) and Middle Tianshan Mountains (MTM). (b) Spatial distribution of the administrative division of the study area. (c) Spatial distribution of land surface types. (d) Spatial distribution of annually averaged accumulative precipitation (shading, units: mm) over the study area in summer (June–August) from 2015 to 2019 and terrain height (gray contours, unit: m).

However, the NSTM is one of the highest-precipitation regions in Xinjiang. A previous research study indicated that in terms of spatial distribution, the precipitation over the Tianshan Mountains accounts for approximately 40.4% of the total precipitation in Xinjiang [24]. Frequent heavy rainfall occurs during the summer season in this region, significantly impacting the area's agriculture, environment, and economy, as well as transportation in the area. Therefore, gaining a thorough understanding of the diurnal variation characteristics in the precipitation patterns over the NSTM is of the utmost importance [25].

Recently, Li et al. [26] conducted a study on the diurnal variation characteristics of summer precipitation over the central Tianshan Mountains based on eight meteorological stations. They found that there were distinct variations in the peak precipitation times across the region: the southern mountain stations experience peak rainfall in the early morning, while the stations near the mountain peaks experience peak rainfall in the evening, and the northern mountain stations show a peak during the nighttime. These variations highlight the significant differences in the precipitation peak characteristics over the regions of the central Tianshan Mountains. Additionally, Cao et al. [27] utilized China ground-based and CMORPH satellite-merged precipitation data to study the diurnal variations in precipitation with different durations during the warm seasons in Xinjiang from 2008 to 2019. The results indicated that precipitation events exceeding 7 h exhibit major peaks that occur in the evening. Furthermore, Cai et al. [28] have begun to explore the long-term effects of oasis expansion on summer precipitation in the northern slope region of the Tianshan Mountains. Their study suggests that oasis expansion contributes to increased summer precipitation in the central Tianshan region.

In previous research studies on the diurnal variation characteristics of precipitation, various types of data were used, such as observation data from meteorological stations [29,30], satellites [31–33], and radars [34] and some reanalysis data [35]. However, due to the limitations in the spatial resolution of the meteorological station data over the NSTM, the detailed diurnal variation characteristics of precipitation, and their behaviors corresponding to the inhomogeneous underlying land surface characteristics remain unclear.

The Advanced Weather Research and Forecasting model improved by Nanjing University (WRF_NJU) has been widely used by scholars in recent years for studying summer precipitation in the central and eastern parts of China. For instance, Xu and Ming [36] pointed out that the diurnal variation trend obtained from the WRF_NJU simulation data is consistent with observations, with peaks occurring at similar times. Additionally, the WRF_NJU simulations perform well for most precipitation events, as stated by Li et al. [37], who also studied the diurnal variation characteristics of precipitation in the Ili Region in Xinjiang. Therefore, in this study, the WRF_NJU data are utilized to investigate the diurnal variation characteristics of precipitation over the NSTM.

The spatial distribution of annually averaged precipitation in summer (accumulated in the period from June to August) obtained from the WRF_NJU data also shows the inhomogeneity of the precipitation pattern in this region (Figure 1d). To better understand the specific diurnal variation characteristics of precipitation related to underlying surface effects, this work focuses on examining the variation characteristics of precipitation at different topographic elevations and over the various land surface categories. This approach aids in accurately understanding the tempo-spatial distributions of the diurnal variation characteristics of precipitation and related possible influencing environmental factors over the NSTM and provides some insights into the possible mechanisms behind precipitation formation and variation characteristics in this region. In addition, this study may also offer a scientific foundation for the evaluation of numerical models and serves as a reference for improving regional precipitation modeling and forecasting.

The remainder of this paper is organized as follows. The data and methods used in this work are described in Section 2, and the main results regarding the NSTM are presented in Section 3. We discuss the results and derive conclusions from them in Sections 4 and 5, respectively.

2. Data and Methods

2.1. Dataset

This study utilized hourly precipitation data from 342 Automatic Weather Stations (AWSs), ERA5-Land reanalysis data, 4 km resolution WRF_NJU data, hourly satellite precipitation data CMORPH with 0.25° resolution, and MSWEP data with 3-h and 0.1° resolution during the summer months (from June to August) for the period from 2015 to 2019. The AWS data were sourced from the National Meteorological Information Center, and rigorous quality control was performed during data processing to ensure accuracy and reliability [38]. The ERA5-Land data were provided by the European Centre for Medium-Range Weather Forecasts. The CMORPH data were created and developed by the NOAA Climate Prediction Center (CPC) via the technique of producing global precipitation products with high spatial and temporal resolutions using joint temporal–spatial interpolation to integrate multi-platform satellite observations [39]. The MSWEP precipitation data have global coverage, and these data have merged various data points sourced from ground-based observations, satellites, and reanalysis data to obtain high-quality precipitation estimates. These two kinds of satellite precipitation products have a wide coverage and are sufficiently time-efficient to compensate for the shortcomings of ground-based rain gauges and ground-based radars [40]. Therefore, these satellite precipitation data were used to validate the performance of the WRF_NJU data over the study area. The simulation results in the 13–36 h forecast period of the WRF_NJU data were used to analyze the precipitation, and the model biases during the early 12-h spin-up period of the simulation were removed or decreased, as recommended by other previous studies [41–43]. The parameterization schemes utilized in the simulation process are detailed in Table 1.

Table 1. List of the parameterization schemes used in the WRF_NJU system used in this work.

Parameterization Scheme	Type
Lateral boundaries	NCEP GFS real-time forecasts at 3-hourly intervals.
Horizontal grid points	1408 × 1080
Grid spacing	4 km
Vertical levels	51
Microphysics	Morrison 2-moment [44]
Planetary boundary layer scheme	Asymmetrical Convective Model version 2 [45]
Land surface and surface layer schemes	Pleim–Xiu [46]
Short- and long-wave radiation schemes	CAM [47]

2.2. Methods

Hourly mean precipitation amount (PA):

$$PA = \sum_{d=1}^n prcp(h, d) / n \quad (1)$$

Hourly mean precipitation frequency (PF):

$$PF = \sum_{d=1}^n pf(h, d) / n \times 100\% \quad (2)$$

Hourly mean precipitation intensity (PI):

$$PI = \frac{PA}{PF} \quad (3)$$

In the above equations, $prcp(h, d)$ represents the precipitation amount at time h on the d day. $pf(h, d) = 1$ indicates that a precipitation of 0.01 mm is counted as an occurrence of precipitation at time h , and $PA < 0.01$ is counted as 0 occurrences. PI indicates the total precipitation amount at a specific time divided by the total number of precipitation occurrences at that time.

The Coefficient of Variation (CV) was utilized to assess the degree of tempo-spatial dispersion of a variable. The CV calculation formula was as follows:

$$CV = \frac{\sigma}{\mu} \times 100\% \quad (4)$$

In the above equation, σ represents the standard deviation of PA, and μ represents the mean value of PA.

Rotated Empirical Orthogonal Function (REOF) analysis was employed to decompose the tempo-spatial distribution patterns of a variable [48]. Additionally, the significance test was conducted using the North methodology [49]. The calculation formula was as follows:

1. Calculate the covariance matrix C :

$$C = \frac{1}{N} X^T X \quad (5)$$

X represents the observation matrix, where each row corresponds to a time step, and each column corresponds to an observed variable. N is the number of samples, and T indicates the transpose of the matrix.

2. Perform an eigenvalue decomposition on the covariance matrix C :

$$C = E \Lambda E^T \quad (6)$$

E is the matrix of eigenvectors, where each column represents an eigenvector. Λ is the diagonal matrix of eigenvalues, with the eigenvalues as the elements along the diagonal.

3. Select the top n eigenvectors (principal components):

From the eigenvalue matrix Λ , choose the eigenvectors corresponding to the n largest eigenvalues to construct the eigenvector matrix E_n .

4. Construct principal component time series:

Project the observation matrix X onto the eigenvector matrix E_n to obtain the matrix of principal component time series P :

$$P = X E_n \quad (7)$$

5. Rotate the principal components:

Select a rotation matrix R (for example, a varimax rotation matrix) and multiply the matrix of principal component time series P by the rotation matrix to obtain the rotated matrix of principal component time series P_{rot} :

$$P_{rot} = P R \quad (8)$$

Taking into account the geographical location of NSTM, the time division is as follows (Table 2):

Table 2. Time slot names and their corresponding time ranges used for the diurnal variation characteristics of precipitation analysis in this paper.

Time Slot Name	Time Range (LST = UTC + 6)
Midnight	2300–0100
Early morning	0200–0400
Dawn	0500–0700
Morning	0800–1000
Noon	1100–1300
Afternoon	1400–1600
Nightfall	1700–1900
Evening	2000–2200

3. Results

3.1. Comparison of Precipitation Characteristics

Figure 2 shows the diurnal variations of spatial distribution of PA over the NSTM at every 6 h (obtained from AWS data, WRF_NJU data, ERA5–Land data, CMORPH data, and MSWEP data). At 0300 Local Solar Time (LST), the spatial distributions of PA obtained by the AWSs (Figure 2a) showed that the higher precipitation (>0.1 mm) is mainly distributed over the MTM (indicated by the large white circle) and showed a precipitation band orientation from the west–northwest to east–southeast (WNW to ESE) directions. However, lower precipitation (<0.02 mm) occurred over the northern part of the study area (i.e., over the Junggar Basin, JB). The distribution of PA obtained by the WRF_NJU (Figure 2b) indicate that, despite some biases in the value of the PA over the eastern part of the MTM and ETM (denoted by small white circle), the overall pattern of the PA is very similar to what is depicted by the AWS data. However, the distribution of PA obtained by the ERA5–Land data (Figure 2i) revealed that the overall distribution of the PA is consistent with that of the WRF_NJU data (except for the high-precipitation region, which seemed to be displaced by about 0.5° to the north, and the value of PA over the ETM is overestimated to degree about 0.05 mm). The distribution of PA obtained from the CMORPH data (Figure 2j) revealed that the center of heavy precipitation (reaching about 0.3 mm) over the MTM is consistent with that of the WRF_NJU data. In addition, the values of PA over the MTM and ETM seemed to be weaker compared to the WRF_NJU results, whereas the distribution of the lower PA obtained from the CMORPH data over the JB was very similar to that of the WRF_NJU data. The distribution of PA obtained by the MSWEP data (Figure 2k) shows a band-shaped precipitation pattern over the MTM and ETM, which is consistent with that of the WRF_NJU data. The pattern and orientation of the precipitation band obtained by the MSWEP data are consistent with that of the WRF_NJU data. Overall, all three datasets showed similar distributions of PA, with a precipitation band orientated in the WNW to ESE direction and almost the same PA strength level over the MTM region of the study area, indicating that the lowest PA (<0.02 mm) occurs over the northern part of the study area over the JB.

By 0900 LST, the distributions of PA obtained by both the AWS and WRF_NJU data (Figure 2c,d) depict a reduction in the value of PA and a contraction of its spatial extent over the MTM region (indicated by the large white circles), and the value of PA in the JB further weakens to some extent. At this time, the distributions of PA obtained by the WRF_NJU data and ERA5–Land data display a consistent overall pattern and are located near the ETM (indicated by the small white circles). The distribution of PA obtained by the CMORPH data (Figure 2m) shows that the precipitation characteristics of the mountainous region are not so obvious, and the precipitation over the JB is still weaker than that of the area over the MTM and ETM, which is consistent with that of the WRF_NJU data. The distribution of PA obtained by the MSWEP data (Figure 2n) shows that the value of the PA over the MTM region has increased and that the spatial coverage has expanded. Additionally, the precipitation over the JB has weakened to some extent, while the precipitation band over the MTM and ETM are consistent with that of the WRF_NJU data and AWS data. The value of the PA over the eastern part of the ETM is overestimated to a degree of about 0.05 mm. The characteristics of the precipitation obtained from these products have similar spatial patterns, but there are differences in the value of the PA. Among them, the results of the MSWEP data showed the best agreement with the observations, and this was also noted in a previous study [50].

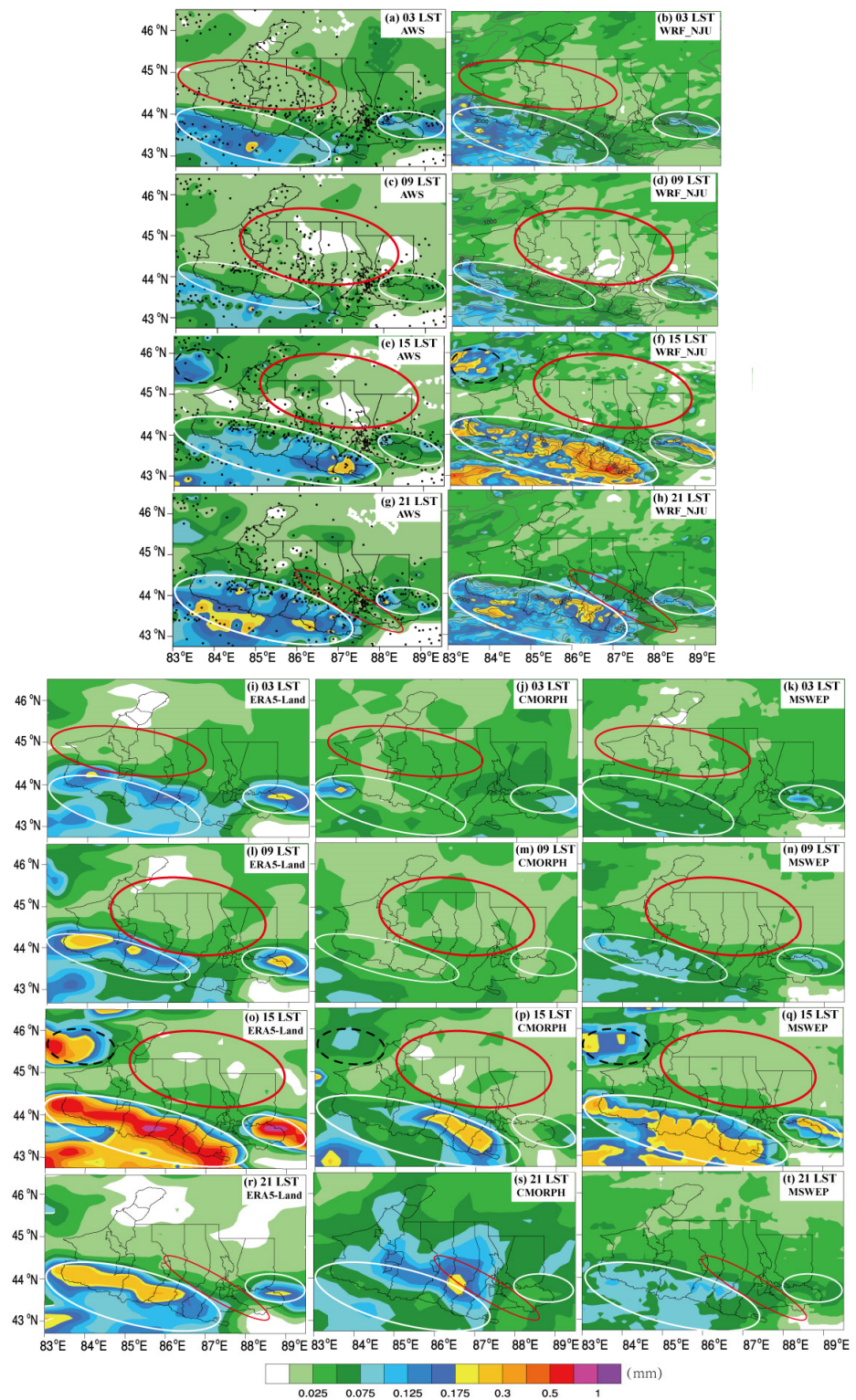


Figure 2. Spatial distribution of average precipitation amount (PA) (shading, units: mm) at 6-h intervals, obtained from (a,c,e,g) Automatic Weather Stations (AWS) data, (b,d,f,h) WRF_NJU data, (i,l,o,r) ERA5-Land data, (j,m,p,s) CMORPH data, and (k,n,q,t) MSWEP data, respectively, over the study area in summer (June–August) from 2015 to 2019. The black lines represent the administrative boundaries, the gray contours depict the terrain altitude, and the small black dots denote the locations of AWSs in the study area. The white and red circles indicate the mountainous areas and rather flat areas with lower altitude, respectively, the black circles indicate the mountainous areas in the NSTM. The specific time is shown in the upper right corner of each panel.

At around 1500 LST, the MTM region experiences the diurnal peak value of PA. In all five datasets (Figure 2e,f,o–q), the distribution of the PA aligns with each other over the mountainous region. The distributions of PA obtained from the WRF_NJU data over the JB below 2000 m ASL (above sea level) are more consistent with that of the AWS data, while the distribution of PA indicated by the AWS data in the mountainous region is rather weak compared to the what is depicted by the WRF_NJU data. This is probably due to the fact that the interpolated distribution pattern of PA revealed by the AWS data is unable to accurately represent the real PA over the relatively sparse distribution of the AWSs over the higher regions above 2000 m ASL in the MTM region. Comparatively, the distribution of PA revealed by ERA5–Land data showed a relatively higher value than that of WRF_NJU data over the mountainous region, which is consistent with previous assessments of PA obtained from the ERA5–Land data over mountainous region of the Qilian Mountains in Northwestern China [51]. The distribution of PA obtained by the CMORPH data (Figure 2p) shows that the value of the PA over the mountainous areas is relatively lower than that of the WRF_NJU data and slightly higher than that of the AWS data. The distribution of PA obtained by the MSWEP data (Figure 2q) shows that the value of the PA over the MTM and ETM roughly coincides with that of the WRF_NJU data, and the distribution of the PA over the mountainous areas outside the study area is consistent with that of the other four datasets (shown by the black dots). By 2100 LST, precipitation in the mountainous regions significantly diminishes across all datasets, while the value of PA over the JB slightly increases (Figure 2g,h,r–t).

It is worth noting that due to the limited distribution of the AWSs over the mountainous region of the NSTM, the spatial distribution results interpolated from the AWS data cannot accurately reflect the PA characteristics over the mountainous areas. Influenced by complex underlying surfaces, the reanalysis data exhibit a systemic overestimation and limited ability to capture fine-scale precipitation variations [51]. This aligns with the findings of Chen et al. [52] in their assessment on the hourly precipitation characteristics in the Qinghai–Tibet Plateau.

It can be concluded from the aforementioned analyses that the distributions of PA and their variation trends in the five datasets are generally consistent. The WRF_NJU model successfully simulates the spatial distribution, intensity, and diurnal variations of precipitation over the NSTM. Similarly, Xu and Ming [36] investigated the performance of the WRF_NJU data for the summer precipitation over Xinjiang, and they found that the diurnal variations of precipitation from the WRF_NJU data are consistent with the observed variations, as the peak periods of precipitation are similar with that of the observation data. In addition, Li et al. [37] studied the diurnal variation characteristics of precipitation in the Ili region based on the same WRF_NJU data, and they also stated that the overall characteristics of precipitation obtained from the WRF_NJU data were consistent with the observation and reanalysis data. Consequently, these data can be considered reliable, as they are going to be employed for future research on the diurnal precipitation characteristics over the NSTM.

3.2. Diurnal Variations in the Spatial Distribution of Precipitation

The spatial distribution of the PA showed a precipitation band orientated from the WNW direction to the ESE direction and an increase in both its extent and intensity from 0600 LST (Figure not shown) to 1500 LST (Figure 2h). The mountainous regions (including both MTM and ETM) reach their PA peaks at around 1500 LST, with precipitation values exceeding 0.5 mm. The distribution of maximum PA aligns with the topography of the Tianshan Mountains. However, there is little variation in PA over the JB, with most regions of JB experiencing values below 0.075 mm (Figure 2h). The PA over the mountainous regions notably weakens during the period from 1800 LST to 0300 LST, decreasing below 0.125 mm. In the southern part of the JB, PA peaks (about 0.175 mm) occur at around 2100 LST (Figure 2k).

As shown in Figure 3, the spatial distribution of PF exhibits significant diurnal variation characteristics. During the period from 0600 to 0900 LST (Figure 3a,3b), the MTM region shows a PF of about 10–20%, while the value of PF over the JB ranges from 5 to 12.5%. The PF over the ETM region is a little higher than that of the eastern part of the MTM region, with the ETM region having a frequency of 12.5–20%. The PF in the central part of the JB decreases to some extent, and the minimum PF is below 5%, which is located near the city of Shihezi (Figure 3b). By 1200 LST, there is a noticeable increase in PF over both the MTM and ETM regions, forming a band-like pattern that roughly aligns with the mountainous terrain, and the PF increases from 15% to 45% (Figure 3c). At around 1500 LST (Figure 3d), the MTM region experiences a significant increase in PF, along with an expansion in its spatial coverage, and the maximum PF exceeds 60%. The PF in the basin area between the MTM and ETM is rather small (with a frequency of 5 to 15%), and it increases in the northern part of the ETM from 30 to 40%. From 1800 LST to 0600 LST (Figure 3e,f), the PF decreases over the MTM region, while the PF gradually increases over the JB. It is evident that the spatial distribution of PF follows a similar diurnal trend to the distribution of the PA. The diurnal variation of PF in the mountain regions is also much greater than those in the basin regions. It is evident that the spatial distribution of PF follows a similar diurnal trend to the distribution of PA. The diurnal variation of PF in mountain regions is also much greater than those in the basin regions.

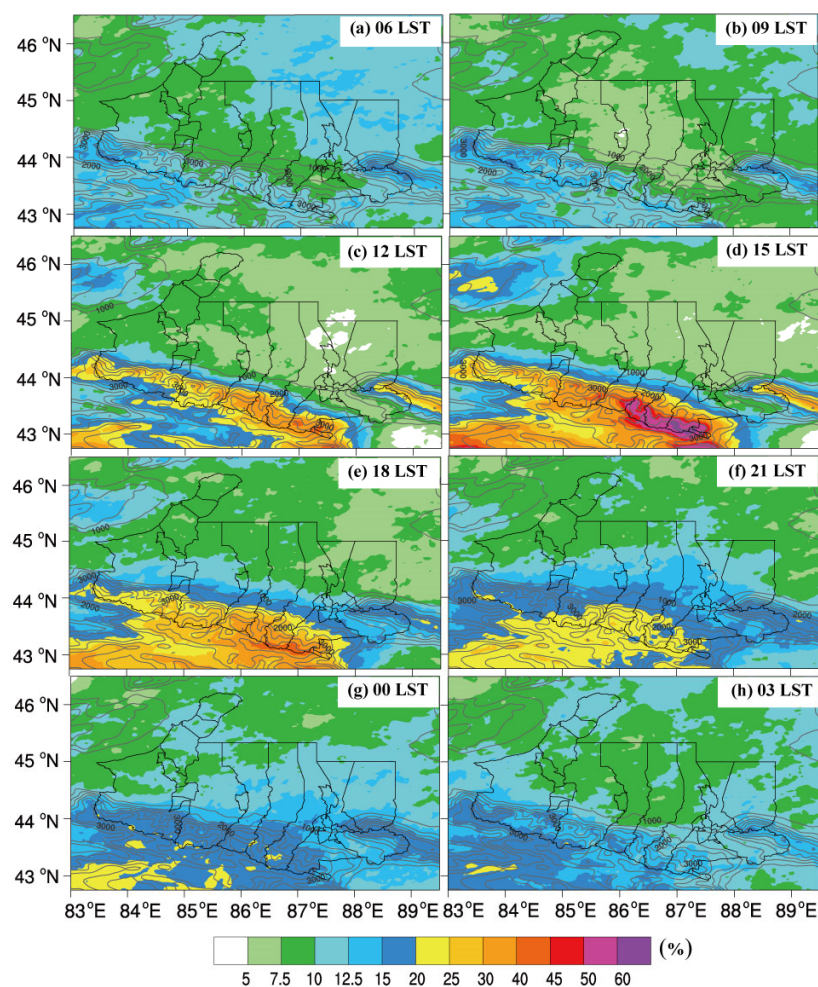


Figure 3. (a–h) Spatial distribution of average precipitation frequency (PF) (shading, units: %) at 3-h intervals over the study area in summer (June–August) from 2015 to 2019 (obtained from WRF_NJU data); the gray contours depict the terrain altitude. The specific time is shown in the upper right corner of each panel.

Precipitation intensity (PI) is an important index to describe the characteristics of precipitation, and the greater the intensity, the fiercer the rain. The PI is noticeably higher along the mountainous regions of the study area compared to the southern parts of the JB during the period between 0600 LST and 1200 LST (Figure 4a–c). At around 1500 LST, the region with PI exceeding 0.5 mm h^{-1} over the study area expands significantly compared to the previous time period. There is also a notable increase in PI over the JB, with some regions experiencing PI between 1 and 1.5 mm h^{-1} (Figure 4a–d). By 1800 LST, the highest PI of the day occurs along the MTM and the ETM regions, reaching values exceeding 1.5 mm h^{-1} (Figure 4e). From 1800 LST to 0000 LST, the PI gradually decreases over the mountainous regions of the MTM and the ETM regions. Meanwhile, the JB experiences PI ranging from 0.4 to 1 mm h^{-1} , exhibiting an eastward movement pattern across the study area (Figure 4e–g). At 0000 LST, the central part of the JB exhibits the highest PI (Figure 4g). By 0300 LST, the PI continues to decrease over the central mountainous regions of the northern slope region of the MTM and the JB. The northern part of the ETM region maintains its intensity, albeit with a reduced spatial coverage (Figure 4h).

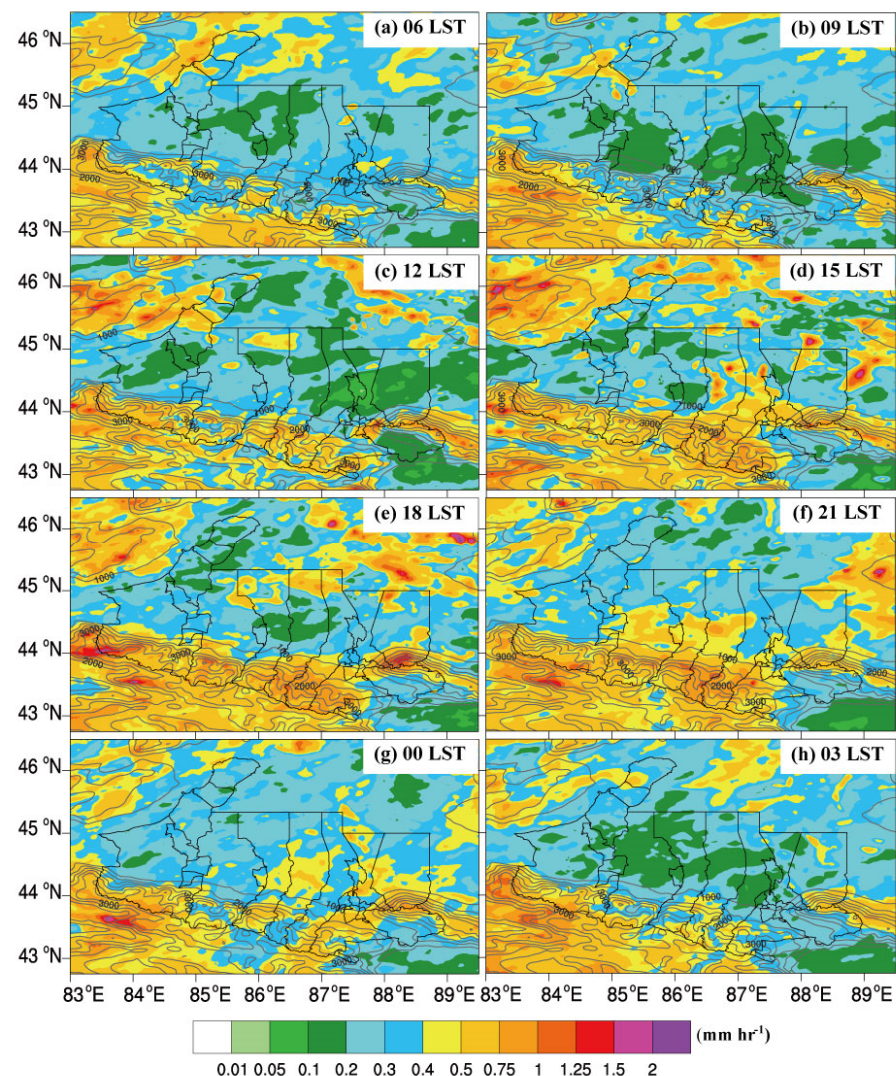


Figure 4. (a–h) Spatial distribution of average precipitation intensity (PI) (shading, unit: mm h^{-1}) at 3-hour intervals over the study area in summer (June–August) from 2015 to 2019 (obtained from WRF_NJU data); the gray contours depict the terrain altitude. The specific time is shown in the upper right corner of each panel.

As shown in Figure 5, we also investigated the spatial distribution characteristics of the diurnal peak time of the precipitation amount (PTPA) in the study area. It can be seen that the PTPA in the study area mainly occurs from the afternoon to the night (i.e., from 1400 LST to 2000 LST). The PK in the southern edge of the JB appears from the night to the early morning (i.e., from 1900 LST to 0600 LST). There is a significant lagging trend in the PTPA from the mountainous regions to JB, along with a west–east lagging trend in the study area. However, the PTPA over the neighboring mountainous region near the northern part of Karamay occurred from midnight to early afternoon (i.e., from 0200 LST to 1500 LST), showing some significant differences from other areas (probably due to complex terrain).

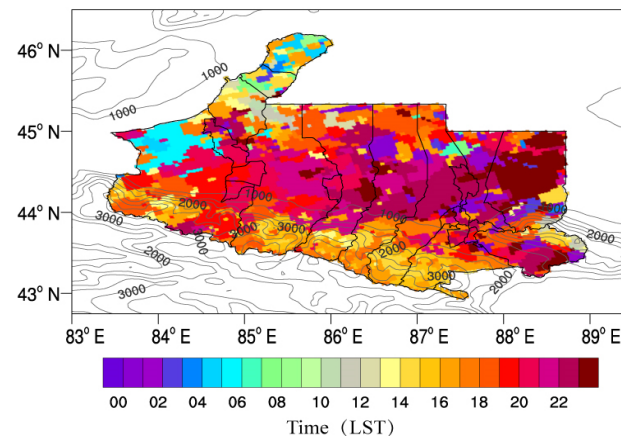


Figure 5. Spatial distribution of diurnal peak time (shading, unit: LST) of the precipitation amount (PA) in summer (June–August) from 2015 to 2019 (obtained from WRF_NJU data); the gray contours depict the terrain altitude (units: m).

Figure 6a shows the diurnal characteristics of PA, PI, and PF averaged over the study area in summer from 2015 to 2019. From the figure, it can be seen that the peak value of PA occurs between 1600 and 1800 LST, and the valley value of PA occurs at 0900 LST. The peak value of PF occurs around 1900 LST, and the valley value of PF occurs at 0900 LST. The daily variation curves of PF and PA are relatively close, showing a distribution feature from afternoon to night that is greater than that from early morning to noon. The peak value of PI occurs in the period between 1500 and 2200 LST, while the valley value of PI occurs between 2300 and 1400 LST, with a peak of 2000 LST and a valley of 0900 LST. The PI shows a gradual increase during the day and the opposite at night. These findings are consistent with the conclusion drawn by Guo et al. [53].

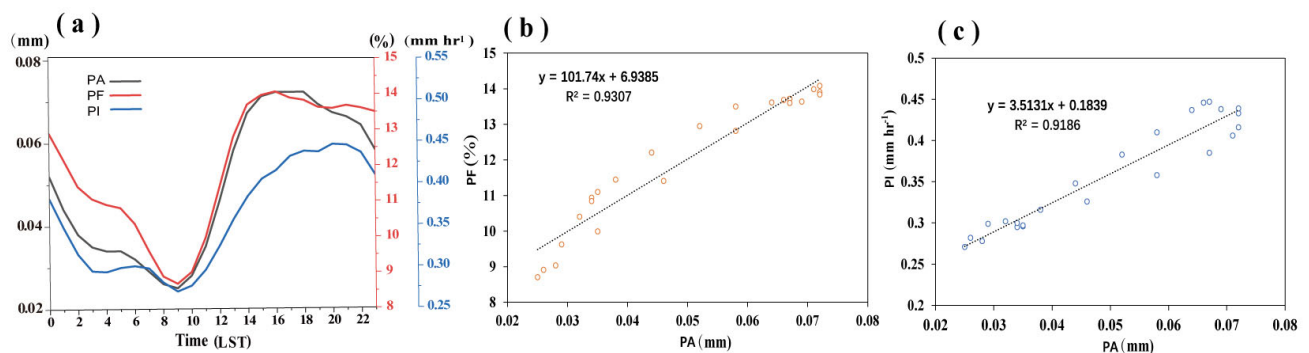


Figure 6. (a) Diurnal variations regarding precipitation amount (PA), precipitation frequency (PF), and precipitation intensity (PI) averaged over the study area in summer (June–August) from 2015 to 2019 (obtained from WRF_NJU data). (b) Scatter plot showing the correspondence of the PA and PF; the dashed line represents the simple linear regression fitting line. (c) Scatter plot showing the correspondence of the PA and PI; the dashed line represents the simple linear regression fitting line.

As can be seen from the scatter plot reflecting the correspondence of the PA and PF (Figure 6b) and PA and PI (Figure 6c), the scatter points are almost evenly distributed on both sides of the simple linear regression fitting line. Additionally, the R^2 of both of the linear regression equations are rather high (>0.9), evidencing the suitable fitting effect of the regression equations. The correlation coefficient between PA and PF is 0.96, and the correlation coefficient between PA and PI is 0.92, indicating that PA has a stronger correlation with PI and PF, and the correlation with PF is a little higher than the correlation with PI.

In this study, following the approach outlined by Karl and Knight [54], the PI characteristics were further analyzed by dividing the PI into 10 levels. According to Figure 7, it is evident that different PI levels contribute differently to the total PA. More than 95% of extreme heavy precipitation events contribute the most to the total PA, accounting for over 60% of the total contribution across all time periods. Moderate to heavy precipitation contributes to over 85% of the total PA in all time periods. During the noon to evening hours, both the occurrence frequency and the contribution to total PA of moderate to heavy precipitation are higher compared to that of the nighttime to morning hours. Particularly at around 1600 LST, the occurrence of precipitation events with intensities exceeding 90% is prominent, constituting around 60% of the total PA.

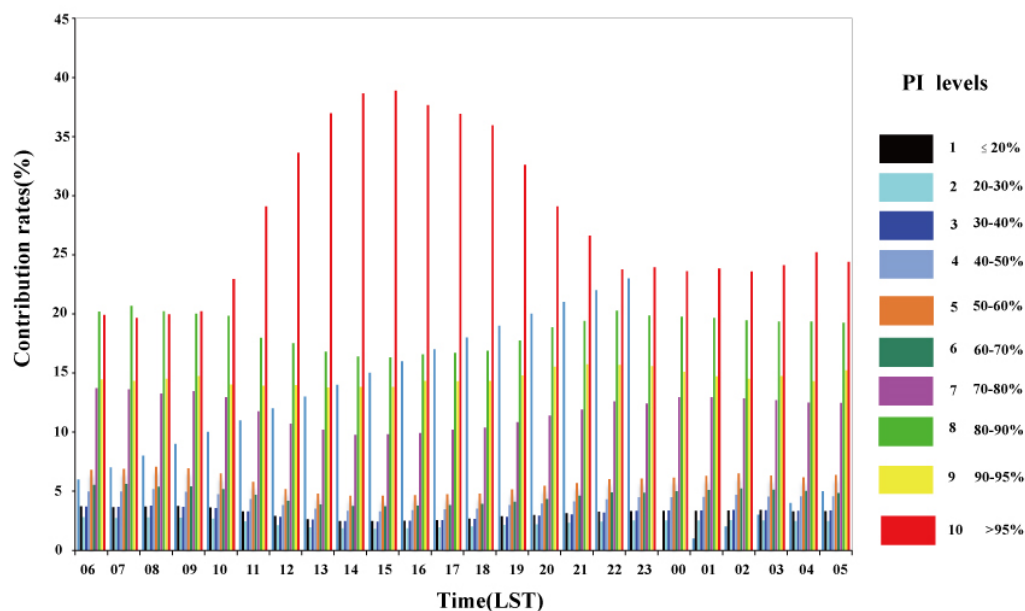


Figure 7. Diurnal variations regarding the contribution rates (unit: %) of the different precipitation intensity (PI) levels in total precipitation averaged over the study area in summer (June–August) from 2015 to 2019 (obtained from WRF_NJU data).

In general, distinct differences exist in the diurnal variation of PA among different PI levels, with a significant contribution from moderate to heavy precipitation. To quantitatively analyze the contribution of different PI levels to the total PA, it was calculated that the cumulative contribution of PI from the 5th to the 10th level constitutes 86.67% of the total PA, with an average PI of 0.81 mm h^{-1} . Notably, the 10th PI level has the highest contribution rate, reaching 28.98% among the 10 levels (see Table 3).

Table 3. Precipitation intensity (PI) (unit: mm h^{-1}) and contribution rates (unit: %) of the different PI levels averaged over the study area in summer (June–August) from 2015 to 2019.

PI Levels	5	6	7	8	9	10	5–10
PI (mm h^{-1})	0.41	0.57	0.82	1.23	2.08	3.10	0.81
Contribution rates (%)	6.03	4.84	12.32	19.39	15.12	28.98	86.67

3.3. REOF and Coefficient of Variation Analysis

In order to clearly express the diurnal variation characteristics of precipitation over the complex terrain conditions in the study area, we employed REOF (Rotated Empirical Orthogonal Function) analysis to perform a tempo–spatial deconstruction of the precipitation characteristics within the study area [24]. Furthermore, a North significance test was conducted [49], and the results indicated that the first three modes had passed the validation test. The cumulative contribution rate of these three modes reached 84%, with the first mode accounting for a variance contribution rate of 66.2%, which significantly exceeded the contribution of the other modes (Figure 8a). The second and third modes exhibited much lower magnitudes compared to the first mode (Figure 8b,c). Therefore, this study predominantly focuses on the first mode to delineate the pronounced diurnal precipitation differences between the mountainous area and basin area of the JB. The first mode effectively captures the tempo–spatial variation characteristics of precipitation in the study area. In this mode, regions with positive values indicate regions of high precipitation, while regions with negative values correspond to regions of low precipitation. The consistent occurrence of precipitation in the northwest mountainous region near the Karamay and the mountainous area over the MTM and ETM suggests a clear pattern of mountainous precipitation. Temporally, the peak of mountainous precipitation mainly occurs around 1500 LST during midday, whereas the peak of precipitation over the JB occurs during 0000~0100 LST (Figure 8d). These differences reflect that the primary causes of the variation characteristics of precipitation within the study area are the topographical (underlying surface) influences.

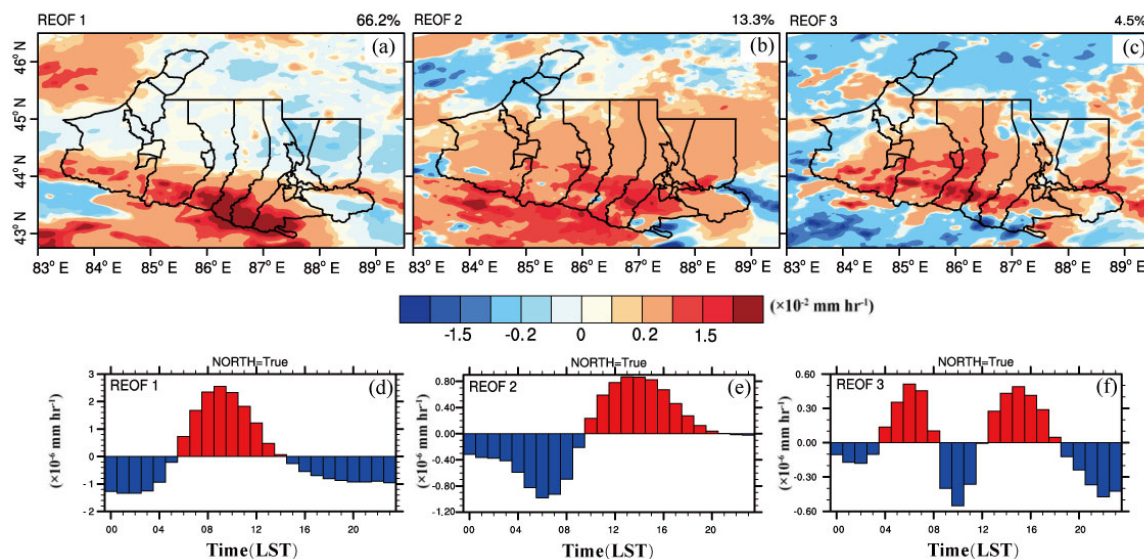


Figure 8. (a–c) Spatial distributions of the first three leading modes of the REOF decomposition of precipitation amount (PA); (d–f) temporal distribution of the amplitudes of temporal weights of the time series of the corresponding modes of the REOF decomposition averaged over the study area in summer (June–August) from 2015 to 2019 (obtained from WRF_NJU data).

The disparities in the diurnal variation characteristics of precipitation across the different regions within the study area are obvious. To delve deeper into these disparities, the coefficients of variation (CV) for both the PF and PI in the study area were calculated. The CV for the PF (Figure 9a) shows that the southern and southeastern part of the JB displays CV values exceeding 40%. The high CV values for these regions indicate that there are significant differences in the daily variability of precipitation, which are closely related to possible weather events [7,37]. However, the western parts of the JB and mountainous areas, including both MTM and ETM, show very low values (below 10%). Referring to the CV for the PI (Figure 9b), it can be seen that the regions characterized by high CV values

for PI include the mountainous regions over the central to eastern MTM and the relatively wide region in the southeastern JB, with the CV value exceeding 80%. The high CV values indicate that there are large variations in PI in these regions, which are susceptible to catastrophic weather events.

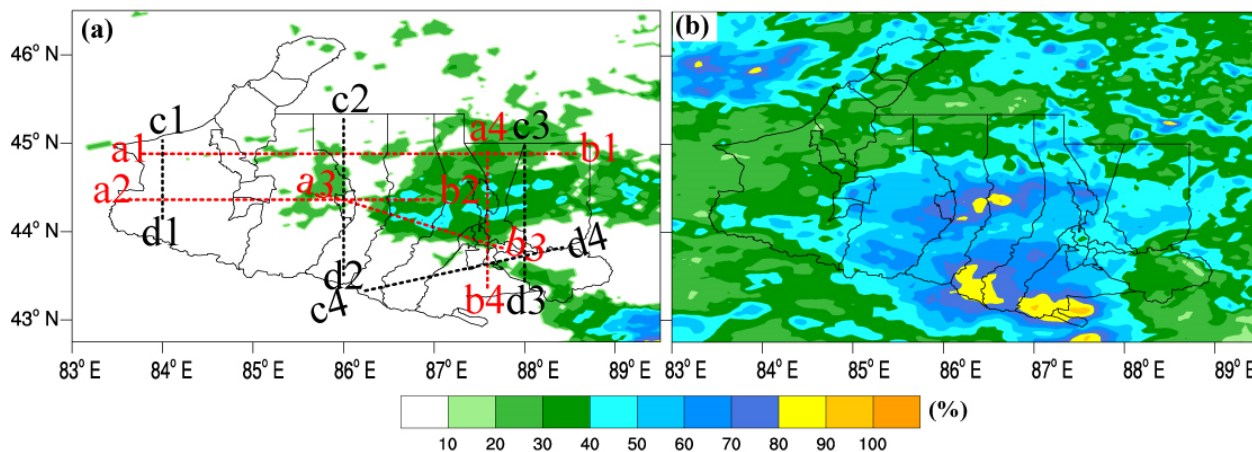


Figure 9. (a) Spatial distribution of the coefficient of variation (CV) (shading, unit: %) for the precipitation frequency (PF) averaged over the study area in summer (June–August) from 2015 to 2019 (obtained from WRF_NJU data). (b) The same as (a) but for the spatial distribution of the coefficient of variation (CV) (shading, unit: %) for the precipitation intensity (PI). The black and red dashed line segments represent the positions of the vertical cross sections in Figures 11 and 13.

3.4. Diurnal Variation Characteristics of Precipitation at Different Altitudes

The findings described in previous publications indicate that there are significant differences in the diurnal variation characteristics of precipitation between mountainous and plain regions [21,28,55,56]. Consequently, we chose intervals of 500 m to calculate the diurnal variation characteristics of precipitation at different altitudes over the study area. As shown in Figure 10a, the most significant characteristics of the overall variation pattern is that the PA notably increases with altitude. Specifically, the time of maximum PA shifts from 2200 LST at 0–500 m altitude to 1800 LST at 1500–2000 m altitude. At above 2000 m, there is a sharp increase in the PA throughout the afternoon, peaking in the early afternoon (1500 LST) from a minimum around of 0800 LST. Overall, the diurnal variation of PA exhibits distinct differences at various altitudes, with a time lag in peak occurrence times from higher altitudes to lower altitudes (i.e., time lag in the timing of peak precipitation from the peaks to the slopes and from the slopes to the basin area).

It can be seen from the diurnal variation characteristics of the PF (Figure 10b) at different altitudes that the highest PF in the range of 0–1500 m altitude occurs at around 2100 LST. At above 2000 m, the PF gradually rises with the increase in altitude, reaching its peak at about 1400–1500 LST, and decreases to the lowest value at around 0800 LST. Similarly, different altitude regions exhibit notable differences in diurnal variation characteristics in PF. At above 1500 m, the PF peaks occurred in the period between 1400 and 1500 LST, lagging by about 5 hours from mountain peaks to slopes and lagging by 2 h from slopes to the JB.

The diurnal variation characteristics of PI are depicted in Figure 10c. At 0–1500 m altitude, the maximum PI occurs at around 2100 LST, and the minimum value occurs at around 0900 LST. For the highest altitudes of 2000–5197 m, the peak PI appears at 1800 LST, while the minimum PI occurs at around 0700–0800 LST. Similarly, different altitude regions show significant differences in the diurnal variation characteristics of PI. The peak intensity of PI lags by about 3 hours from higher altitudes to lower altitudes, shifting by 2 h from slopes to the JB (Figure 10c).

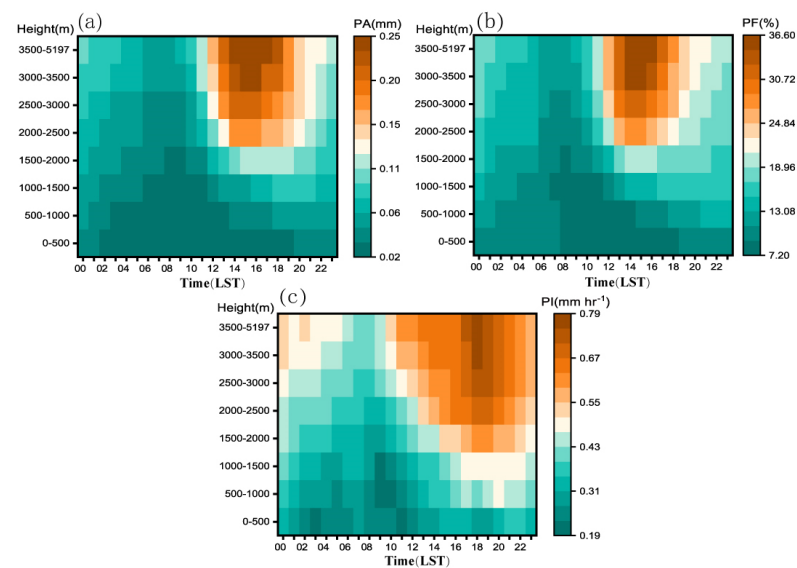


Figure 10. (a) Diurnal variations regarding the precipitation amount (PA) averaged over the study area in summer (June–August) from 2015 to 2019 at different altitudes (obtained from WRF_NJU data). (b,c) The same as (a) but for the precipitation frequency (PF) and precipitation intensity (PI), respectively.

In order to further investigate the diurnal variation characteristics of precipitation over the inhomogeneous underlying regions in the study area, we conducted further analyses on some vertical cross sections (shown in Figure 9a) over some of the inhomogeneous underlying regions.

As shown in Figure 11a, there is a clear topographical inhomogeneity (in the high topography, i.e., mountains, in the south and low topography, i.e., basin, and in the north) along the cross section c1d1, which is located in the western part of the study area. In general, the PA increases gradually from basin to mountains in this cross section. The PA over the basin area is less than 0.04 mm, with the peak time in terms of precipitation amount (PTPA) being 2100 LST. The PTPA over the area from the foothill to the hillside occurs at around 1500–1800 LST, and the PA exceeds 0.2 mm over the mountainous region at this time. The topographic features shown in Figure 11b are roughly similar to those in Figure 11a, with high altitude (mountains) in the south and low altitude (basin) in the north. The PTPA occurs at 1200 LST over the area near the northern ending point (i.e., c2) of line segment c2d2, while the overall PTPA over the other basin and hill side area below ~3300 m occurs at 2100 LST. However, the PTPA over the mountainous region above ~3300 m occurs at 1500 LST, reaching a maximum value of ~0.3 mm.

Along the vertical cross section of c3d3 (Figure 11c), located in the eastern part of the study area, the value of PA over the basin area remains below 0.06 mm. The PTPA over the area near the northern ending point (i.e., c3) occurs at 1800 LST, while the other basin and near foothill area below ~1200 m experiences the PTPA at 0000 LST. However, the PTPA over the mountainous region above ~1400 m occurs at 1800 LST.

As for the cross section along the line segment gone through the canyon area between the MTM and ETM (i.e., c4d4 in Figure 11d, both ending points of the line segment are located over the mountains), the peak value of PA over the mountainous area of MTM above 3100 m reached ~0.35 mm at 1500 LST, while the peak value of PA is only about 0.18 mm over the top of the ETM (occurring at about 1800 LST). The PTPA occurs at around 1500–1800 LST over the western mountainous area (MTM) above 1800 m, while the PTPA over the small part of the hillside area at about 1400–1700 m altitude occurs at 2100 LST. However, the canyon area below 1400 m and its adjacent area up to the top of the ETM experienced the PTPA at 1800 LST.

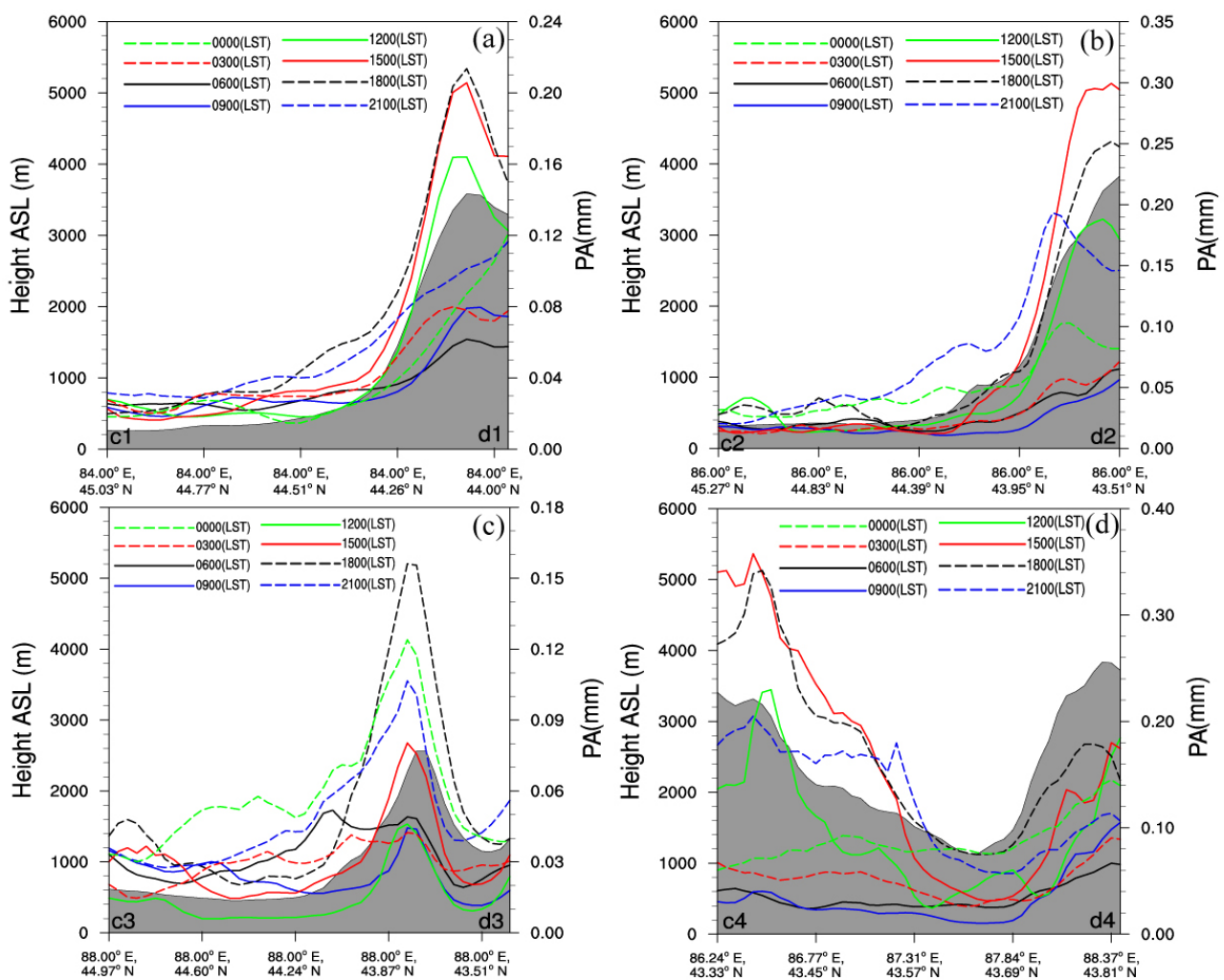


Figure 11. (a–d) Distribution of the precipitation amount (PA) (contours, units: mm) at 3-h intervals along the different line segments (shown in Figure 9) in the study area in summer (June–August) from 2015 to 2019 (obtained from WRF_NJU data); the gray shading indicates the terrain altitude (units: m).

In general, the PA over the mountainous regions is significantly higher than those in the low-altitude regions (i.e., the JB, foothill, or canyon regions). The PTPA in the mountains regions occurs in the afternoon to evening, while the low-altitude regions experiences the PTPA from late evening to early morning, with a lower peak PA value.

3.5. Diurnal Variation Characteristics of Precipitation on Different Land Surface Categories

Some previous studies have found significant differences in the characteristics of precipitation on different land surface categories over uniform-altitude regions [57]. Therefore, we also investigated the diurnal variation characteristics of precipitation on different land surface categories in the study area.

For the sake of simplicity, the major six land surface categories in the study area were selected to analyze the corresponding diurnal variation characteristics of precipitation. As shown in Figure 12a, the PTPA occurs at 1500–1600 LST over the forests, with the highest value of PA being about 0.179 mm h^{-1} . The PTPA occurs at 1600 LST over the grasslands and watersheds, with the highest values of PA being about 0.109 mm h^{-1} and 0.099 mm h^{-1} , respectively. Previous studies [16] regarding the diurnal variation of precipitation in the central Amazon Basin have shown that the rainfall over the forests are 20% greater than those over the urban area during the afternoon hours; this is because the humidity in

the boundary layer over the forests is kept at high levels due to the transpiration by the forests, thereby providing more water vapor for the occurrence of precipitation. It can be deduced that the relatively high PA over the forests and grassland is also caused by a relative increase in water vapor in the boundary layer due to vegetational transpiration. Similarly, water bodies have a high evaporation capacity, which leads to more water vapor in the boundary layer, thereby favoring the occurrence of precipitation. However, due to the relatively small size of the water bodies in the study area, the PA over the water bodies is slightly lower compared to those over the forests and grassland. The PTPA occurs at 2000–2200 LST (0.053 mm h^{-1}) for impervious surfaces, 1700 LST (0.052 mm h^{-1}) and 2200 LST (0.046 mm h^{-1}) for waste bodies, and 2100 LST (0.049 mm h^{-1}) for cropland. From nighttime to midday, the PA was higher in the waste bodies than in the cropland and impervious surfaces. In the afternoon, the PA was lower in barren land than in the cropland and impervious surfaces.

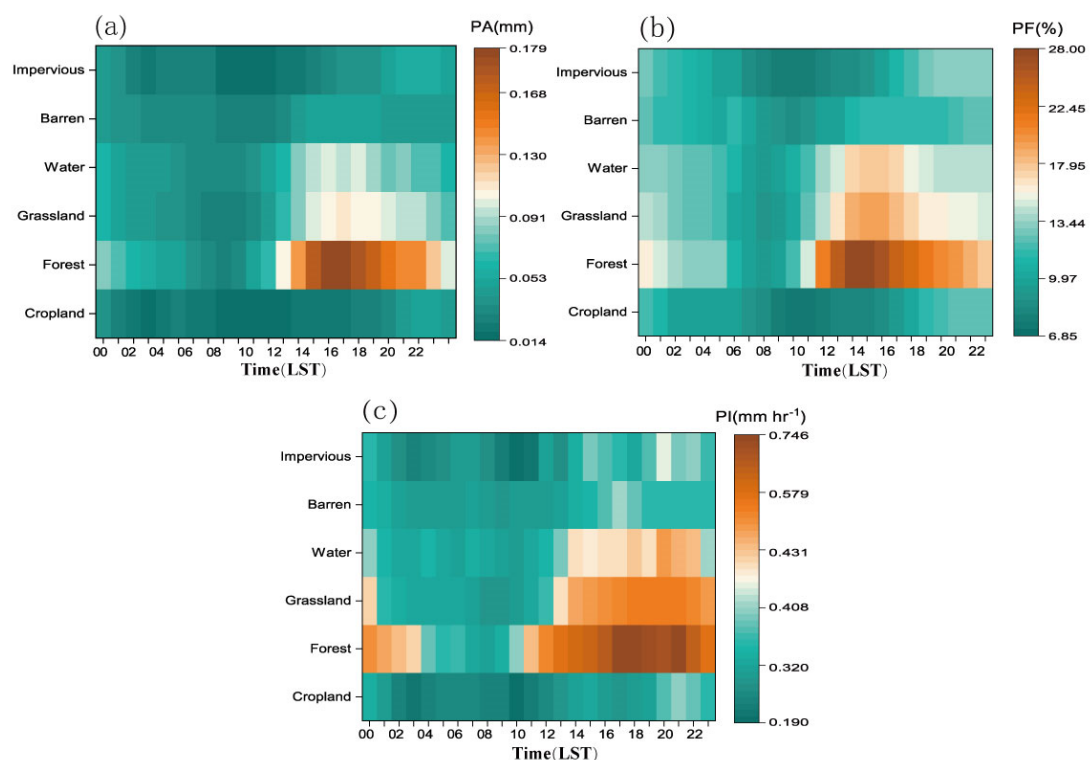


Figure 12. (a) Diurnal variations regarding the precipitation amount (PA) averaged over several major land surface categories in the study area in summer (June–August) from 2015 to 2019 (obtained from WRF_NJU data). (b,c) The same as (a) but for the precipitation frequency (PF) and precipitation intensity (PI), respectively.

The diurnal variation characteristics of PF (Figure 12b) over the different land surface categories exhibit roughly similar patterns to that of the PA. The forests have the highest PF, which occurs earlier than that of other categories in the day. Grasslands and water bodies have the second and third highest PF values, while impervious surfaces, cropland, and waste bodies have the lowest PF values, with the peaks occurring later in the day. The diurnal variation characteristics of PI (Figure 12c) of various land surface categories also show distinct diurnal variations. The forests exhibit the highest PI, whereas grasslands and water bodies have relatively weaker PI. Impervious surfaces, croplands, and waste bodies experience the weakest PI. For all six land surface categories, PI shows the lowest (highest) value in the early morning (nighttime) hours.

In order to further investigate the specific diurnal variation characteristics of precipitation over the different land surface categories, further analyses on some vertical cross sections (shown in Figure 9a) over some of the different land surface categories were

conducted. As can be seen in Figure 13a, prominent diurnal variation characteristics in precipitation can be found in profile a1b1 (Figure 13a). Referring to the administrative divisions in Figure 1b and the land surface categories in Figure 1c, it can be seen that the line segment of a1b1 is far away from urban areas and that the topography is relatively flat. However, the diurnal variation characteristics of precipitation exhibit distinct fluctuations. This is probably due to the alternative distribution of barren lands and croplands along the line segment a1b1. The maximum PA over the croplands in the north of Wusu is less than 0.04 mm, peaking at 1500 LST. For the barren lands and croplands north of Manas, the barren lands north of Hutubi, and the grasslands north of Changji, the maximum precipitation is less than 0.04 mm, with peaks at 1800 LST and 0000 LST. The barren lands north of Urumqi and Fukang have a maximum precipitation of about 0.07 mm, peaking at 0000 LST.

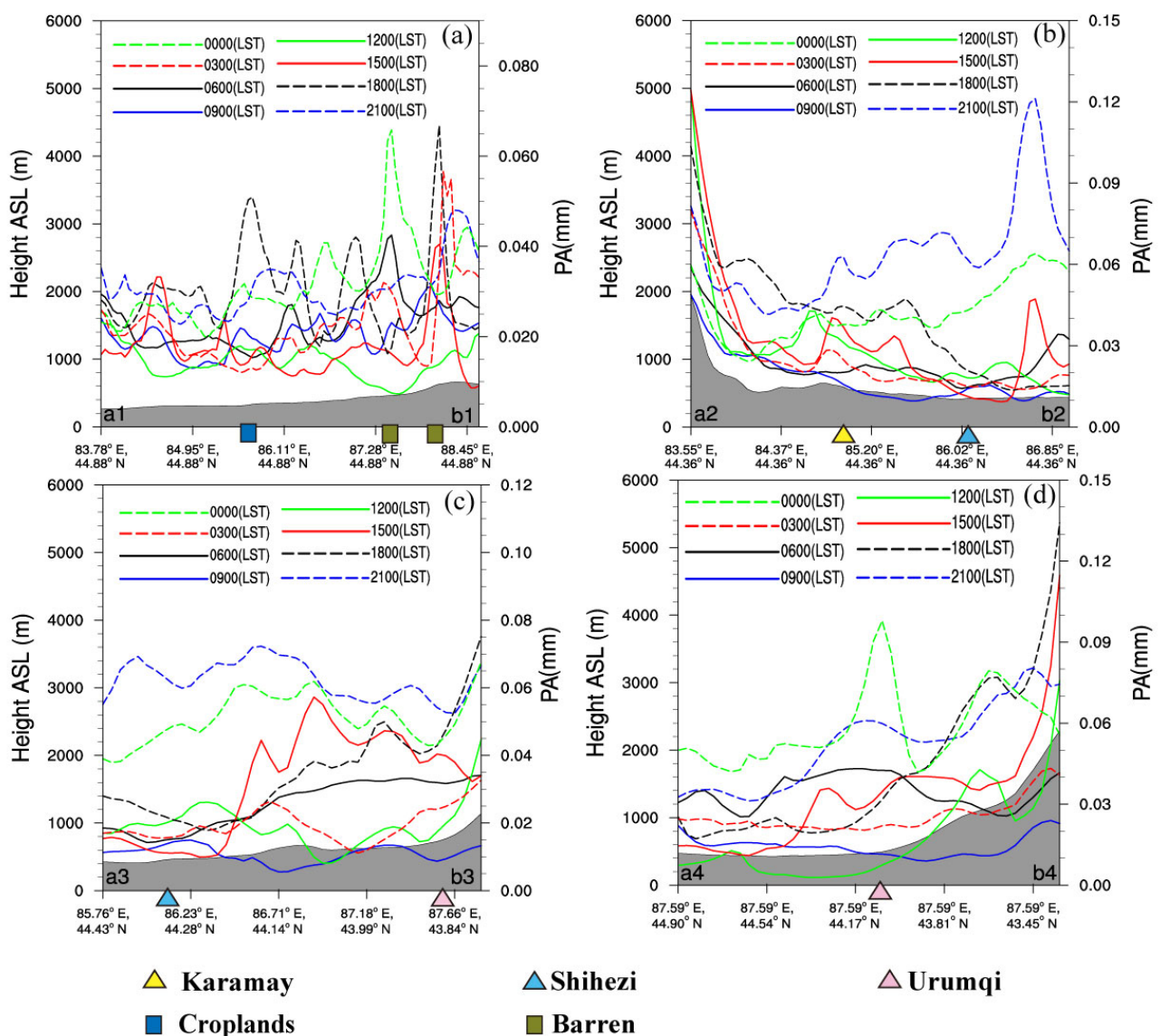


Figure 13. (a–d) Diurnal variations regarding the precipitation amount (PA) at 3-h intervals along the different line segments (shown in Figure 9) which went through the major land surface categories in the study area in summer (June–August) from 2015 to 2019 (obtained from WRF_NJU data); the gray shading indicates the terrain altitude (units: m). The colored triangles indicate the locations of the major cities located on the line segments, and the colored small boxes represent the location of croplands and barren lands on the line segments.

As can be seen from the vertical cross section along a2b2 (Figure 13b), the locations of the two triangular marks indicate the locations of urban areas of Karamay and Shihezi, and the PTPA occurs at 2100 LST, with a value of about 0.06–0.07 mm. The easternmost part of this cross section experiences the peak PA (up to about 0.12 mm) at 2100 LST (roughly higher than the cropland of Hutubi), and the minimum value of the PA occurs at 0900 LST. It is worth noting that most of the contours of PA (except for those at 0600 and 0900 LST) show a slightly increasing pattern (i.e., convex shape) over these two cities (significantly above the Karamay), indicating that urbanization possibly has an effect on the precipitation.

The southern part of the cross section along line segment a3b3 (Figure 13c) is the urban area of Shihezi, and the central part is the cropland in central Hutubi. The maximum PA is up to 0.072 mm (occurring at 2100 LST). The southeastern Urumqi urban area experienced the maximum PA at 2100 LST (up to about 0.06 mm) and minimum PA at 0900 LST. The southernmost precipitation peak of the PA (up to about 0.125 mm) occurs over the farmland of Hutubi, the PTPA occurs at 2100 LST, and the minimum value of PA occurs at 0900 LST.

As for Figure 13d, the line segment of a4b4 runs from north to south through Urumqi, the largest city in Xinjiang. The topography is high in the south and low in the north. The maximum PA peak is located in the center of Urumqi, where the precipitation exceeds 0.1 mm (probably due to the urban heat island effect), with the peak occurring around 0000 LST. The PA increases rapidly as the elevation rises towards the south, with 0.13 mm in the mountainous areas roughly above 2000 m, with the peak occurring at 1800 LST. However, the influence of topography on PA seems to be much greater than that of the land surface categories.

4. Discussion

This study mainly employed hourly WRF_NJU data from the summer months (June–August) of five continuous years (2015–2019) with 4 km resolution to conduct an in-depth investigation into the diurnal variation characteristics of precipitation over the northern slope of the Tianshan Mountains (NSTM), Xinjiang. Due to the relatively sparse population, complex terrain, and harsh environment within the study (such as desert and Gobi), the number or density of conventional and automatic weather stations in Xinjiang are much less than that of the mid-eastern part of China. Therefore, we felt that the 1 h and 4 km resolution simulation data from a consecutive 5-year time range could undoubtedly provide a good opportunity to investigate the much more detailed characteristics of diurnal variation of precipitation in the region. The WRF_NJU data distinctly elucidate the tempo–spatial evolution characteristics and peak features of precipitation amount (PA), precipitation frequency (PF), and precipitation intensity (PI), facilitating a thorough understanding of the mechanisms behind the intricate diurnal precipitation patterns over the complex underlying surfaces in the region. Unlike previous research studies that have primarily relied on a limited number of automated meteorological station observations to analyze the diurnal variation characteristics of precipitation in the NSTM [58–60], this study reveals that the majority of the region experiences peak PA in the afternoon to evening hours, whereas the peak in the Junggar Basin (JB) occurs during the late evening to early morning hours. These kind of differences may be due to the influence of the different topographies in these areas. The noticeable delay in peak PA (due to topography) indicates significant regional disparities, and there is a distinct eastward propagation trend of peak timing in the JB.

In addition, this study has uncovered substantial disparities between the diurnal variations of precipitation on the NSTM and other mountainous regions in China [17,56,61]. In the NSTM, the regions with higher elevations exhibit higher values of PA, PF, and PI [51,55]. Notably, there are distinct temporal differences in the peak time of PA, PF, and PI between the mountainous regions and the JB, with an overall single-peak characteristic. In contrast, the high-altitude regions of the eastern Qinghai–Tibet Plateau (southeastern plateau, northern Hengduan Mountains, and transitional zone between high and low elevations) and the diurnal variation characteristics of precipitation in the Sichuan Basin

exhibit single peaks during the nighttime [62], while other regions (southeastern Yungui Plateau and southern Hengduan Mountains) manifest a bimodal structure [41]. In contrast to urban agglomerations in eastern China, the cities in the study area are small in scale, and except for Urumqi, the diurnal variation characteristics of precipitation in other cities cannot be clearly affected by the urban underlying surface [19].

Furthermore, for this study, we employed Regional Empirical Orthogonal Function (REOF) analysis, and the first mode of decomposed precipitation pattern revealed the tempo–spatial variation patterns of diurnal precipitation on the NSTM rather well. This analysis highlighted the divergent diurnal precipitation characteristics between the mountainous regions and the JB and the variations associated with different land surface categories [16,32,57]. The Coefficient of Variation (CV) results indicate that high-value regions are primarily distributed in the mountainous regions, exceeding 80%, significantly surpassing those in the Sichuan Basin and southern China [62,63]. This reflects the pronounced regional discrepancies in the diurnal variations of precipitation in the NSTM and its susceptibility to hazardous weather. Notably, previous studies on precipitation in the NSTM have predominantly focused on intense precipitation events in individual cases [11,64,65]. We believe that this work provides valuable insights into the mechanisms underlying isolated precipitation events in the region.

5. Conclusions

This paper evaluated the modeling capability of a convection-resolvable model with a horizontal resolution of 4 km for summer precipitation in the NSTM. The diurnal variation characteristics of precipitation in the NSTM were revealed based on these high-resolution simulation data. The main conclusions that can be drawn from this study are as follows:

(1) The WRF_NJU data accurately simulated the diurnal variation characteristics of precipitation over the NSTM. Compared to observational data, the ERA5 reanalysis data are essentially similar in terms of PA. Due to the sparse distribution of the AWSs in the NSTM, it is challenging to reasonably reflect the precipitation characteristics of the mountainous regions. Meanwhile, the precipitation obtained from the ERA5 data exhibits a systematic overestimation and struggles to capture fine-scale variations in precipitation.

(2) The diurnal variation characteristics of precipitation in the mountainous regions exhibit a pronounced unimodal characteristic, with the peak PA primarily occurring in the late afternoon. The PA decreases during the night, reaching its minimum value from early morning to morning. The annual average accumulated precipitation in the JB is significantly lower than that in the mountainous regions, with the maximum PA occurring from evening to early morning. Within the study area, the tempo–spatial distribution of hourly averaged PA, PF, and PI are closely aligned, with correlations all exceeding 90%.

(3) The diurnal variation characteristics of precipitation differ noticeably at different altitudes. In the JB, below 1000 m, the PA peak occurs at 2200 LST. In the mountainous regions above 3000 m, the PA reaches its peak in the afternoon at 1500 LST, with the PF showing a similar trend. The peak PI in the mountainous regions occurs at 1200 LST, while the PI appears at around 1600 LST in the JB.

(4) The mountainous regions and the JB in the NSTM exhibit distinct diurnal variations in precipitation, which are prominently more influenced by topography compared to land surface categories. The peak of the PA in the mountainous regions predominantly occurs around noon at 1500 LST, while in the JB, the peak arises between 0000 and 0100 LST. High CV values were exhibited by the central JB and the central Tianshan Mountain regions, indicating significant diurnal variation characteristics in precipitation. This variability suggests an increased likelihood of extreme rainfall events.

(5) The precipitation peaks for forests, grasslands, and water bodies all occur between 1500 and 1600 LST, whereas for impervious surfaces, croplands, and barren lands, the peaks are between 2000 and 2200 LST. The peaks of PF in forests, grasslands, and water bodies appear at 1000 LST. In contrast, those for impervious surfaces, croplands, and barren lands appear at 1700 LST. The intensity peaks for forests and barren lands occur at 1200 LST,

while those for water bodies, impervious surfaces, grasslands, and croplands appear at 1500 LST.

Author Contributions: Data curation: Z.K., Z.L., D.A. and K.Z.; formal analysis: Z.K. and Z.L.; investigation: Z.K., Z.L., A.A. (Abidan Abuduaini) and A.A. (Abuduwaili Abulikemu); methodology: Z.K., Z.L. and A.A. (Abuduwaili Abulikemu); project administration: A.A. (Abuduwaili Abulikemu); resources: K.Z. and Z.L.; software: Z.K., Z.L. and A.A. (Abuduwaili Abulikemu); supervision: A.A. (Abuduwaili Abulikemu); validation: Z.K., Z.L. and A.A. (Abuduwaili Abulikemu); writing—original draft: Z.K., Z.L. and A.A.; writing—review and editing: Z.K., Z.L., A.A. (Aerzuna Abulimiti) and A.A. (Abuduwaili Abulikemu). All authors have read and agreed to the published version of the manuscript.

Funding: This work was sponsored by the Natural Science Foundation of Xinjiang Uygur Autonomous Region (2022D01C359), the National Natural Science Foundation of China (42265003), the National Key Research and Development Program of China (2018YFC1507103), the 100 Young Doctors Introduction Program of Xinjiang (Tianchi Doctor Program) Foundation (50500/04231200737), and the Doctoral Research Startup Foundation of Xinjiang University (50500/62031224618).

Data Availability Statement: The hourly surface automatic weather station dataset was collected and compiled by the China Meteorological Administration (CMA); WRF_NJU provided by Key Laboratory of Mesoscale Severe Weather of Nanjing University. The ERA5–Land reanalysis dataset from the European Center for Medium–Range Weather Forecasts (ECMWF) was used in this study to provide auxiliary data ([https://cds.climate.copernicus.eu/cdsapp#!/dataset/reanalysis-\\$Sera5-\\$Land?tab=form](https://cds.climate.copernicus.eu/cdsapp#!/dataset/reanalysis-$Sera5-$Land?tab=form), accessed on 15 December 2022). The land surface type and topographic data were sourced from the Resource and Environmental Science and Data Center of the Chinese Academy of Sciences (<https://www.resdc.cn/>).

Acknowledgments: We thank the four anonymous reviewers and all editors for their valuable comments, suggestions and efforts during the handling of our manuscript. We also thank for the High-Performance Computing Center of Nanjing University for conducting the numerical calculations in this paper on their IBM Blade cluster system.

Conflicts of Interest: The authors declare no conflict of interest.

References

1. Jeong, J.-H.; Walther, A.; Nikulin, G.; Chen, D.; Jones, C. Diurnal cycle of precipitation amount and frequency in Sweden: Observation versus model simulation. *Tellus A Dyn. Meteorol. Oceanogr.* **2011**, *63*, 664–674. [[CrossRef](#)]
2. Li, X.; Lau, N.-C.; Lee, T.-C. An Observational Study of the Diurnal Variation of Precipitation over Hong Kong and the Underlying Processes. *J. Appl. Meteorol. Climatol.* **2018**, *57*, 1385–1402. [[CrossRef](#)]
3. Dai, A.; Deser, C. Diurnal and semidiurnal variations in global surface wind and divergence fields. *J. Geophys. Res. Atmos.* **1999**, *104*, 31109–31125. [[CrossRef](#)]
4. Dai, A.; Giorgi, F.; Trenberth, K.E. Observed and model-simulated diurnal cycles of precipitation over the contiguous United States. *J. Geophys. Res. Atmos.* **1999**, *104*, 6377–6402. [[CrossRef](#)]
5. Lynn, J.; Peeva, N. Communications in the IPCC’s Sixth Assessment Report cycle. *Clim. Chang.* **2021**, *169*, 18. [[CrossRef](#)] [[PubMed](#)]
6. Yuan, W. Diurnal cycles of precipitation over subtropical China in IPCC AR5 AMIP simulations. *Adv. Atmos. Sci.* **2013**, *30*, 1679–1694. [[CrossRef](#)]
7. Li, D.; Sun, J.; Fu, S.; Wei, J.; Wang, S.; Tian, F. Spatiotemporal characteristics of hourly precipitation over central eastern China during the warm season of 1982–2012. *Int. J. Climatol.* **2016**, *36*, 3148–3160. [[CrossRef](#)]
8. Ombadi, M.; Risser, M.D.; Rhoades, A.M.; Varadharajan, C. A warming-induced reduction in snow fraction amplifies rainfall extremes. *Nature* **2023**, *619*, 305–310. [[CrossRef](#)]
9. Abulikemu, A.; Wang, Y.; Gao, R.; Wang, Y.; Xu, X. A Numerical Study of Convection Initiation Associated with a Gust Front in Bohai Bay Region, North China. *J. Geophys. Res. Atmos.* **2019**, *124*, 13843–13860. [[CrossRef](#)]
10. Abulikemu, A.; Xu, X.; Wang, Y.; Ding, J.; Wang, Y. Atypical occlusion process caused by the merger of a sea-breeze front and gust front. *Adv. Atmos. Sci.* **2015**, *32*, 1431–1443. [[CrossRef](#)]
11. Kong, M.; Abulikemu, A.; Zheng, J.; Aireti, M.; An, D. A Case Study on Convection Initiation Associated with Horizontal Convective Rolls over Ili River Valley in Xinjiang, Northwest China. *Water* **2022**, *14*, 1017. [[CrossRef](#)]
12. Patz, J.A.; Campbell-Lendrum, D.; Holloway, T.; Foley, J.A. Impact of regional climate change on human health. *Nature* **2005**, *438*, 310–317. [[CrossRef](#)] [[PubMed](#)]
13. Xiao, C.; Yuan, W.; Yu, R. Diurnal cycle of rainfall in amount, frequency, intensity, duration, and the seasonality over the UK. *Int. J. Climatol.* **2018**, *38*, 4967–4978. [[CrossRef](#)]

14. Carbone, R.E.; Tuttle, J.D.; Ahijevych, D.A.; Trier, S.B. Inferences of predictability associated with warm season precipitation episodes. *J. Atmos. Sci.* **2002**, *59*, 2033–2056. [[CrossRef](#)]
15. Wang, C.-C.; Huang, H.-L.; Li, J.-L.; Leou, T.-M.; Chen, G.T.-J. An Evaluation of the Performance of the CWB NFS Model for Warm-Season Rainfall Distribution and Propagation over the East Asian Continent. *Terr. Atmos. Ocean. Sci.* **2011**, *22*, 49–69. [[CrossRef](#)] [[PubMed](#)]
16. Tanaka, L.M.d.S.; Satyamurty, P.; Machado, L.A.T. Diurnal variation of precipitation in central Amazon Basin. *Int. J. Climatol.* **2014**, *34*, 3574–3584. [[CrossRef](#)]
17. Li, L.; Li, J.; Chen, H.; Yu, R. Diurnal Variations of Summer Precipitation over the Qilian Mountains in Northwest China. *J. Meteorol. Res.* **2019**, *33*, 18–30. [[CrossRef](#)]
18. Rui, Y.; Shuliang, Z.; Peng, S.; Yaojin, B.; Qiqi, Y.; Zongkui, G.; Yaru, Z. Diurnal Variations in Different Precipitation Duration Events over the Yangtze River Delta Urban Agglomeration. *Remote Sens.* **2022**, *14*, 5244. [[CrossRef](#)]
19. Fu, X.; Yang, X.Q.; Sun, X. Spatial and Diurnal Variations of Summer Hourly Rainfall over Three Super City Clusters in Eastern China and Their Possible Link to the Urbanization. *J. Geophys. Res. Atmos.* **2019**, *124*, 5445–5462. [[CrossRef](#)]
20. Wang, Z.; Liu, S. Estimation and spatiotemporal evolution of groundwater storage on the northern slope of the Tianshan Mountains over the past three decades. *Acta Geogr. Sin.* **2023**, *78*, 1744–1763. [[CrossRef](#)]
21. Zhou, C.; Zhao, C.X.; Yang, Z.P. Strategies for environmentally friendly development in the Northern Tianshan Mountain Economic Zone based on scenario analysis. *J. Clean. Prod.* **2017**, *156*, 74–82. [[CrossRef](#)]
22. Fang, C.; Gao, Q.; Zhang, X.; Cheng, W. Spatiotemporal characteristics of the expansion of an urban agglomeration and its effect on the eco-environment: Case study on the northern slope of the Tianshan Mountains. *Sci. China Earth Sci.* **2019**, *62*, 1461–1472. [[CrossRef](#)]
23. Nie, C.; Qin, C. Study on Intimidation of Water Resources on Urbanization of City Group in the Northern Slope of Tianshan Mountain. *Yellow River* **2020**, *42*, 57–62. [[CrossRef](#)]
24. Shi, Y.; Sun, Z.; Yang, Q. Characteristics of Area Precipitation in Xinjiang Region with Its Variations. *J. Appl. Meteorol. Sci.* **2008**, *19*, 326–332.
25. Chen, C.; Wang, J.; Tang, Y.; Mao, W. Diurnal Variations of Summer Precipitation in Xinjiang. *J. Appl. Meteorol. Sci.* **2017**, *28*, 72–85. [[CrossRef](#)]
26. Li, J.; Chen, T.; Li, N. Diurnal Variation of Summer Precipitation across the Central Tian Shan Mountains. *J. Appl. Meteorol. Climatol.* **2017**, *56*, 1537–1550. [[CrossRef](#)]
27. Cao, J.; Ma, S.; Yuan, W.; Wu, Z. Characteristics of diurnal variations of warm-season precipitation over Xinjiang Province in China. *Atmos. Ocean. Sci. Lett.* **2022**, *15*, 100113. [[CrossRef](#)]
28. Cai, P.; Hamdi, R.; Luo, G.; He, H.; Zhang, M.; Termonia, P.; De Maeyer, P. Agriculture intensification increases summer precipitation in Tianshan Mountains, China. *Atmos. Res.* **2019**, *227*, 140–146. [[CrossRef](#)]
29. Yu, R.; Zhou, T.; Xiong, A.; Zhu, Y.; Li, J. Diurnal variations of summer precipitation over contiguous China. *Geophys. Res. Lett.* **2007**, *34*, L01704. [[CrossRef](#)]
30. Li, J.; Yu, R.; Zhou, T. Seasonal Variation of the Diurnal Cycle of Rainfall in Southern Contiguous China. *J. Clim.* **2008**, *21*, 6036–6043. [[CrossRef](#)]
31. Zhou, T.; Yu, R.; Chen, H.; Dai, A.; Pan, Y. Summer Precipitation Frequency, Intensity, and Diurnal Cycle over China: A Comparison of Satellite Data with Rain Gauge Observations. *J. Clim.* **2008**, *21*, 3997–4010. [[CrossRef](#)]
32. Chen, G.; Sha, W.; Iwasaki, T. Diurnal variation of precipitation over southeastern China: Spatial distribution and its seasonality. *J. Geophys. Res.* **2009**, *114*, D13103. [[CrossRef](#)]
33. Chen, G.; Sha, W.; Iwasaki, T. Diurnal variation of precipitation over southeastern China: 2. Impact of the diurnal monsoon variability. *J. Geophys. Res.* **2009**, *114*, D21105. [[CrossRef](#)]
34. Chen, M.; Wang, Y.; Gao, F.; Xiao, X. Diurnal variations in convective storm activity over contiguous North China during the warm season based on radar mosaic climatology. *J. Geophys. Res. Atmos.* **2012**, *117*, D20115. [[CrossRef](#)]
35. Chen, C.-S.; Lin, Y.-L.; Zeng, H.-T.; Chen, C.-Y.; Liu, C.-L. Orographic effects on heavy rainfall events over northeastern Taiwan during the northeasterly monsoon season. *Atmos. Res.* **2013**, *122*, 310–335. [[CrossRef](#)]
36. Xu, R.; Ming, J. Evaluation of precipitation forecasts from NJU 4 km forecasting system in Xinjiang during summer. *J. Meteorol. Sci.* **2022**, *42*, 804–815.
37. Li, Z.; Abulikemu, A.; Zhu, K.; Mamtimin, A.; Zeng, Y.; Li, J.; Abulimiti, A.; Kadier, Z.; Abuduaini, A.; Li, C.; et al. Diurnal Variation Characteristics of Summer Precipitation and Related Statistical Analysis in the Ili Region, Xinjiang, Northwest China. *Remote Sens.* **2023**, *15*, 3954. [[CrossRef](#)]
38. Shen, Y.; Xiong, A.; Wang, Y.; Xie, P. Performance of high-resolution satellite precipitation products over China. *J. Geophys. Res.* **2010**, *115*, D02114. [[CrossRef](#)]
39. Zang, H.; Wang, Y.; Li, Z. *American Systems for Earth Observation Satellite Data Products and Services*; China Meteorological Press: Beijing, China, 2011; pp. 19–199.
40. Liao, R.; Zhang, D.; Shen, Y. Validation of Six Satellite-Derived Rainfall Estimates over China. *Meteorol. Mon.* **2015**, *41*, 970–979. [[CrossRef](#)]

41. Zhang, Y.; Xue, M.; Zhu, K.; Zhou, B. What Is the Main Cause of Diurnal Variation and Nocturnal Peak of Summer Precipitation in Sichuan Basin, China? The Key Role of Boundary Layer Low-Level Jet Inertial Oscillations. *J. Geophys. Res. Atmos.* **2019**, *124*, 2643–2664. [[CrossRef](#)]
42. Zhu, K.; Xue, M.; Yang, N.; Zhang, C. How Well Does 4-km WRF Model Predict Three-Dimensional Reflectivity Structure over China as Compared to Radar Observations? *J. Geophys. Res. Atmos.* **2023**, *128*, e2022JD038143. [[CrossRef](#)]
43. Zhu, K.; Xue, M.; Zhou, B.; Zhao, K.; Sun, Z.; Fu, P.; Zheng, Y.; Zhang, X.; Meng, Q. Evaluation of Real-Time Convection-Permitting Precipitation Forecasts in China During the 2013–2014 Summer Season. *J. Geophys. Res. Atmos.* **2018**, *123*, 1037–1064. [[CrossRef](#)]
44. Morrison, H.; Curry, J.A.; Khvorostyanov, V.I. A New Double-Moment Microphysics Parameterization for Application in Cloud and Climate Models. Part I: Description. *J. Atmos. Sci.* **2005**, *62*, 1665–1677. [[CrossRef](#)]
45. Pleim, J.E. A Combined Local and Nonlocal Closure Model for the Atmospheric Boundary Layer. Part I: Model Description and Testing. *J. Appl. Meteorol. Climatol.* **2007**, *46*, 1383–1395. [[CrossRef](#)]
46. Pleim, J.E. A Simple, Efficient Solution of Flux–Profile Relationships in the Atmospheric Surface Layer. *J. Appl. Meteorol. Climatol.* **2006**, *45*, 341–347. [[CrossRef](#)]
47. Collins, W.D.; Rasch, P.J.; Boville, B.A.; Hack, J.J.; Mccaa, J.R.; Williamson, D.L. *Description of the NCAR Community Atmosphere Model (CAM 3.0)*; University Corporation for Atmospheric Research: Boulder, CO, USA, 2004; p. 226.
48. Unal, Y.S.; Deniz, A.; Toros, H.; Incecik, S. Temporal and spatial patterns of precipitation variability for annual, wet, and dry seasons in Turkey. *Int. J. Climatol.* **2012**, *32*, 392–405. [[CrossRef](#)]
49. North, G.R.; Bell, T.L.; Cahalan, R.F. Sampling Errors in the Estimation of Empirical Orthogonal Functions. *Mon. Weather Rev.* **1982**, *7*, 699–706. [[CrossRef](#)]
50. Bai, P.; Liu, X. Evaluation of Five Satellite-Based Precipitation Products in Two Gauge-Scarce Basins on the Tibetan Plateau. *Remote Sens.* **2018**, *10*, 1316. [[CrossRef](#)]
51. He, M.; Chen, H.; Yu, R. Evaluation of Warm-Season Rainfall Diurnal Variation over the Qilian Mountains in Northwest China in ERA5 Reanalysis. *Atmosphere* **2022**, *13*, 674. [[CrossRef](#)]
52. Chen, T.; Li, J.; Zhang, Y.; Chen, H.; Li, P.; Che, H. Evaluation of Hourly Precipitation Characteristics from a Global Reanalysis and Variable-Resolution Global Model over the Tibetan Plateau by Using a Satellite-Gauge Merged Rainfall Product. *Remote Sens.* **2023**, *15*, 1013. [[CrossRef](#)]
53. Guo, Y.Z.Y.; Zhang, T.; Yao, J.; Gu, Z. Diurnal Variation of Summer Extreme Precipitation in Tianshan Mountains of Xinjiang. *Desert Oasis Meteorol.* **2023**, *17*, 44–51.
54. Karl, T.R.; Knight, R.W. Secular trends of precipitation amount, frequency, and intensity in the United States. *Bull. Am. Meteorol. Soc.* **1998**, *79*, 231–241. [[CrossRef](#)]
55. Min, Y.; Huang, W.; Ma, M.; Zhang, Y. Simulations in the Topography Effects of Tianshan Mountains on an Extreme Precipitation Event in the Ili River Valley, China. *Atmosphere* **2021**, *12*, 750. [[CrossRef](#)]
56. Zhang, Y.; Hanati, G.; Danierhan, S.; Liu, Q.; Xu, Z. Evaluation and Comparison of Daily GPM/TRMM Precipitation Products over the Tianshan Mountains in China. *Water* **2020**, *12*, 3088. [[CrossRef](#)]
57. Tian, P.; Jian, B.; Li, J.; Cai, X.; Wei, J.; Zhang, G. Land-Use-Change-Induced Cooling and Precipitation Reduction in China: Insights from CMIP6 Models. *Sustainability* **2023**, *15*, 12191. [[CrossRef](#)]
58. Kavitha, M.; Nair, P.R.; Girach, I.A.; Aneesh, S.; Sijikumar, S.; Renju, R. Diurnal and seasonal variations in surface methane at a tropical coastal station: Role of mesoscale meteorology. *Sci. Total Environ.* **2018**, *631–632*, 1472–1485. [[CrossRef](#)] [[PubMed](#)]
59. Li, J. Hourly station-based precipitation characteristics over the Tibetan Plateau. *Int. J. Climatol.* **2018**, *38*, 1560–1570. [[CrossRef](#)]
60. Prein, A.F.; Gobiet, A. Impacts of uncertainties in European gridded precipitation observations on regional climate analysis. *Int. J. Climatol.* **2017**, *37*, 305–327. [[CrossRef](#)]
61. Song, Z.; Zhang, J. Diurnal Variations of Summer Precipitation Linking to the Topographical Conditions over the Beijing-Tianjin-Hebei Region. *Sci. Rep.* **2020**, *10*, 9701. [[CrossRef](#)]
62. Cao, B.; Yang, X.; Li, B.; Lu, Y.; Wen, J. Diurnal Variation in Cloud and Precipitation Characteristics in Summer over the Tibetan Plateau and Sichuan Basin. *Remote Sens.* **2022**, *14*, 2711. [[CrossRef](#)]
63. Fu, S.; Li, D.; Sun, J.; Si, D.; Ling, J.; Tian, F. A 31-year trend of the hourly precipitation over South China and the underlying mechanisms. *Atmos. Sci. Lett.* **2016**, *17*, 216–222. [[CrossRef](#)]
64. Abulikemu, A.; Ming, J.; Xu, X.; Zhuge, X.; Wang, Y.; Zhang, Y.; Zhang, S.; Yu, B.; Aireti, M. Mechanisms of Convection Initiation in the Southwestern Xinjiang, Northwest China: A Case Study. *Atmosphere* **2020**, *11*, 1335. [[CrossRef](#)]
65. Zeng, Y.; Yang, L.; Zhang, Y. Numerical Simulation of Mesoscale System during a Rare Torrential Rainstorm Process in Yili of Xinjiang. *J. Arid Meteorol.* **2020**, *38*, 290–300.

Disclaimer/Publisher’s Note: The statements, opinions and data contained in all publications are solely those of the individual author(s) and contributor(s) and not of MDPI and/or the editor(s). MDPI and/or the editor(s) disclaim responsibility for any injury to people or property resulting from any ideas, methods, instructions or products referred to in the content.